Retrieval of Total Water Vapour Content from MERIS Measurements

Algorithm Theoretical Basis Document

ATBD 2.4

Jürgen Fischer, Ronny Leinweber and Rene Preusker

Free University Berlin
Institute for Space Science

Contents

1. INTRODUCTION

Acronyms and Abbreviations

AERONET   Aerosol Robotic Network
ARM US   Atmospheric Radiation Measurement program
ATBD   Algorithm theoretical basis document
AATSR   Advanced Along Track Scanning Radiometer (ESA)
BRDF   Bi-directional Reflectance Distribution Function
BSRN   Baseline Surface Radiation Network
CDR   Critical Design Review
DUE   Data User Element of the ESA Earth Observation Envelope Programme
ECSS   European Cooperation for Space Standardization
EO   Earth Observation
ENVISAT   Environmental Satellite, ESA
HITRAN   High-resolution transmission molecular absorption database
H2O   Water vapour
IWV   Integrated Water Vapour
MERIS   Medium Resolution Imaging Spectrometer (ESA)
MODIS   Moderate resolution imaging spectrometer (NASA)
MOMO   Matrix Operator Model
NetCDF   Network Common Data Format
NOAA   National Oceanic and Atmospheric Administration
NWP   Numerical Weather Prediction
O2   Oxygen
PDF   Probability Density Function
PDR   Preliminary Design Review
QA   Quality Assessment
QR   Qualification Review
RB   Requirements Baseline document
RD   Reference Document
SLSTR   Sea and Land Surface Temperature Radiometer
TOA   Top Of Atmosphere

Purpose and Scope

This ATBD describes the retrieval of water vapour above from MERIS measurements above land, ocean and clouds.

Algorithm Identification

Columnar water vapour path over land, water and clouds: MERIS_wv_land, MERIS_wv_water and MERIS_wv_cloud. However, as there is no cloud processing branch then the above cloud is for pixels that are not classified as land or water.

2. ALGORITHM OVERVIEW

The water vapour retrieval algorithms dedicated for MERIS are based on the work of [7] and [2]. The general algorithm approach is to relate the columnar water vapour content to the ratio of MERIS channels M14 and M15 located at 885nm and 900nm, respectively. The retrieval will be performed using a neural network which was trained with results of the below described radiative transfer model MOMO. Although conventional regression approaches for model inversion have successfully been applied to the inverse problem, the use of neural networks in this context will lead to significant improvements in the quality of the retrieval. This is especially the case for the low- and high end of the observed water vapour contents, where regression type algorithms typically lead to biases, because of their overall minimization. It further allows us to derive estimates on the quality of the retrieval, which allows us to accept (or reject) the derived retrieval as being consistent (or inconsistent) with the neural network's training data. In contrast to simple regression techniques no threshold techniques have to be applied and pixels, which e.g. have undergone an erroneous cloud classification in the pre-processing will be rejected from the neural network itself as inconsistent with the expected range of data.

2.1.   Physics of the Problem and Sensitivity Studies

Within the spectral range $\rho\sigma\tau$-water vapour absorption band around 935nm exhibits strong absorption by water vapour. The transmission of two model atmospheres within the spectral range relevant for MERIS band M15 is shown in Figure . The water vapour retrieval is based on the principle of differential absorption technique: the amount of absorption A (and accordingly the amount of transmission T) of light at a specific wavelength λ is related to the total mass m of the transmitted absorbing constituents and its mass extinction coefficient $k(\lambda)$.

$$T = 1 - A \propto \ln(m \cdot k)$$

For the remote sensing of atmospheric water vapour using satellite measurements within the solar spectral range of the $\rho\sigma\tau$-band around 935 nm this relation is of little use since many physical properties of the atmosphere and the surface complicate the upper relationship.

1. The effective photon path length can be shortened or extended in a very complex way, depending on the brightness of the surface, the optical thickness of the atmospheric aerosol and the vertical profile of the aerosols.
2. The estimation of the transmission T from the ratio of two close channels (one within and one outside the absorbing band of water vapour) is distorted, when the corresponding surface reflectances differ.
3. The mass extinction coefficients depend on pressure and temperature of the atmosphere.

To estimate the impact of the upper effects on the water vapour retrieval, a set of sensitivity studies are performed. All calculations have been performed for constant observation geometry (sun angle = 35.6°, viewing angle = 0° and azimuth angle = 141.4°) and a medium water vapour amount of 30kg/m² or 30mm. In literature the water vapour amount is given in g/cm², kg/m² and mm, which can easily transferred by a factor of 10 when the unit is changed from g/cm² to

kg/m² and equals when mm is used instead of kg/m². The products of the described water vapour algorithms use the unit kg/m². However, a few figures are still given in mm.
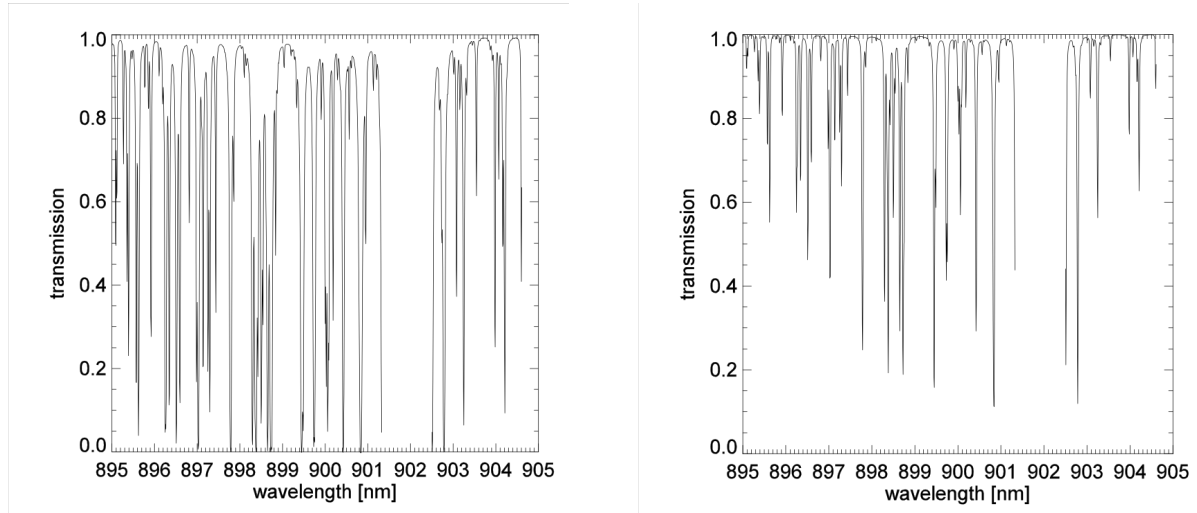
Figure 1: Atmospheric transmission between 895nm an 905nm for two standard atmospheres (left: mid latitude summer, right: arctic winter) calculated from the HITRAN-2000 database

Firstly, we determined the impact of the spectral albedo; for this study the spectral surface albedos for channel M14 and M15 are changed.
Fehler! Verweisquelle konnte nicht gefunden werden. shows the results of the simulations where the x- and y-axes indicates the albedo at 885nm (band 14) and its deviation from the albedo at 900nm (band 15), respectively. The colours show the equivalent change in IWV (Integrated Water Vapour) where the albedo difference is not taken in consideration. One can see that the variations in the water vapour decrease with increasing albedo values. Small variations in the difference of the spectral albedo lead for surface albedos starting from 0.1 to large differences in the IWV of up to 9mm. Especially for low surface albedos, the knowledge of the spectral variance of the surface albedo is very important for the accuracy of the water vapour retrieval.

For the performed radiative transfer simulations the pressure and temperature profiles according to the US-standard atmosphere as well as the different aerosol properties have been chosen.

Figure 3 shows the change in the equivalent IWV as a function of albedo and the change in the temperature and pressure profiles. One can see that variations in the pressure profile leads to differences of up to 1mm in the IWV. The effect of the temperature profile is with a change of 0.8mm weak.
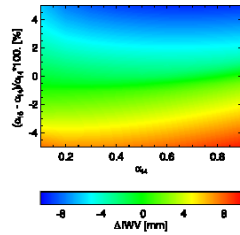
Figure 2: Equivalent change in IWV as a function of the spectral surface albedo, while the considered IWV is 30kg/m². α_{14} is the surface albedo of channel M14 and $(\alpha_{15}-\alpha_{14})/\alpha_{14}*100$ the difference between the spectral albedo for channel M15 and channel M14 in percentage.

Figure 3: Equivalent change of IWV as a function of albedo in MERIS channel M14 (α_{14}) with respect to temperature and pressure changes relative to the US-standard atmosphere. The stars representing a desert and the diamonds a subarctic winter (SAW) temperature profile. The change in surface pressure of +/-10% is illustrated by the triangle and square line, respectively.

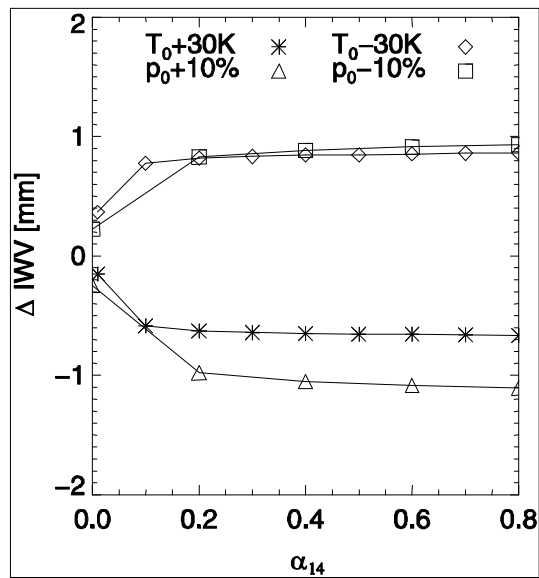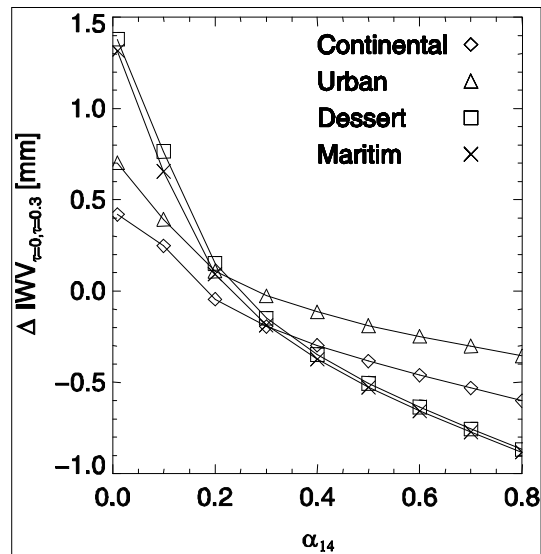**Figure 4: Equivalent change in IWV as a function of surface albedo α_{14}; The aerosol optical thickness have been increased from $\tau=0$ and $\tau=0.3$ for all aerosol types.**

Figure 4 shows the sensitivity of the equivalent IWV for four different aerosol types. The x- and y-axes indicates the albedo and the differences in the equivalent change in IWV computed with an aerosol optical thickness of 0 and 0.3, respectively.

The results of the sensitivity studies are summarized in Table 1 and listed with decreasing influence on the IWV retrieval. It can be seen that the spectral albedo has the strongest influence of the retrieved water vapour. The impact of the temperature profile is less, but might be considered in future evolutions of the algorithm. So far, the water vapour algorithm for land surfaces will consider the impacts due to spectral surface albedo and photon path length by using:

1. The oxygen absorption (MERIS M10 and M11) and the surface pressure as a measure for the photon path length deviation from the geometrical path length.
2. Surface albedo maps using the products of ESA's ALBEDOMAP project (Fischer et al, 2009).
3. The surface pressure (as for 1).

Table 1: Summary of the sensitivities studies tabulating the maximum difference in equivalent IWV for the varying environmental parameters.

	Maximum equivalent change in IWV
Spectral albedo (±5%)	9.0mm
Pressure profile (+/-10%)	1.0mm
Aerosol optical thickness (0 - 0.3)	1.5mm
Temperature profile (+/-30K)	0.8mm

Outside the sun glitter, water surfaces show a significantly lower surface reflectivity in the near infrared with the result that measured signals over water surfaces are governed by aerosol

scattering. The effects of variable aerosol optical depth and of variations in aerosol and water vapour vertical profiles are the most significant factors affecting the retrieval accuracy. Within the sun glitter region, the measured signal is comparable to that above land surfaces and the accuracy of the retrievals over sun glitter is expected to be comparable to land surfaces.

Clouds are bright targets with small spectral variation in reflectivity. Water vapour retrieval results under cloudy conditions are therefore expected to be feasible. Variations in penetration depth of the incoming solar radiation lead to uncertainties in the assignment of the measured water vapour content to an altitude range. The penetration depth is mainly governed by the ratio between cloud optical depth and cloud geometrical thickness. The issues associated with variable penetration depth are closely related to cloud top pressure retrieval and are discussed in more detail in [13, 15]. Another factor, limiting the retrieval accuracy, is the comparably low water vapour content available above high clouds which generally leads to an increasing relative error with increasing cloud top height.

3. ALGORITHM DESCRIPTION

3.1. Algorithm development

The algorithms provided are based on inverse radiative transfer (RT) modelling. A large dataset of different atmospheric profiles of water vapour, temperature, pressure and aerosol types as well as vertical distributions are used as input parameters for the radiative transfer simulations. This input dataset virtually covers the global variability of these parameters. In the subsequent sections the RT model as well as the physical input parameters for the simulations are described.

3.1.1. Matrix Operator Model

The radiative transfer code MOMO [8], [6] was used to simulate the radiances for the MERIS channels. The Matrix Operator Method [14] offers the possibility of a) combination of layers of any given optical properties b) very fast calculation even in the case of optically thick layers with highly anisotropic phase functions c) choice of any desired surface reflectivity, and d) the calculation of up-and down-welling radiances within the ocean and the atmosphere for all layer boundaries. Scattering and absorption processes due to aerosols and cloud particles are represented by appropriate scattering and extinction coefficients and the corresponding scattering phase function. These parameters are obtained by Mie theory. Air molecules are small compared to the wavelength of the incoming sunlight. Thus the molecular scattering can be described with Rayleigh theory. MOMO has been validated by comparisons with other radiative transfer codes as well as with spectral radiation measurements [20].

The calculation of the gas absorption is based on the HITRAN-2000 dataset [18], which contains parameters of the single absorption lines of the main atmospheric gases. The absorption coefficients of the atmospheric gases are calculated with a line-by-line model. The integrated absorption coefficients of individual spectral domains or channels are estimated by a k-binning method [4][3].

3.1.2. Radiative transfer simulations for the algorithm development

Several thousand azimuthally resolved radiance spectra were calculated, covering a broad range of atmospheric temperature and pressure profiles, aerosol optical depths, surface reflectivity values and total water vapour contents both above land and water surfaces as well as clouds. The vertical structure of the atmosphere was described by 22 homogeneous model layers. The input parameters of the simulations are described in some detail in the following sections.

3.1.3. Vertical temperature, pressure and water vapour profiles

Vertical profiles of temperature, pressure and water vapour were taken from worldwide radio soundings, covering a wide range of natural variations. The selected 399 profiles represent a broad range of surface pressure, temperature and water vapour profiles whereby the IWV ranges from 3 to 60 mm. The surface temperature varies between -11.5 to 33.2 °C and surface pressure from 986.9 to 1024.3 hPa. For high surface elevations and the resulting low surface pressure, the coefficients of the proposed water vapour algorithm have to be adapted.

3.1.4. Aerosol optical parameters

Aerosol types, vertical distribution, and optical depth are varied randomly. For each simulation four different aerosol types were considered, stratospheric, tropospheric background, and

maritime (ocean surface) or continental (land surface) aerosol. All atmospheric constituents were allowed to vary randomly within the natural range of variability, as shown in Table 2.

Table 2: Variations in aerosol parameters.

Type	Min. opt. depth	Max. opt. depth
Stratospheric	0.005	0.01
Trop. Background	0.01	0.09
Maritime (ocean)	0.03	0.23
Continental (land)	0.01	0.40

3.1.5. Spectral surface reflectance

The absolute value and the spectral behaviour of the surface reflectance have a distinct impact on the water vapour retrieval (Fischer, 1988). For the present simulations reflectance measurements with high spectral resolution of different targets are taken, whereby the reflectance varies between 10% and 100% [5]. Different types of vegetation, snow and soil are considered. The surface reflectances depend on wavelength in a nonlinear way. Variations are due to spatially and temporally highly variable parameters as e.g. chlorophyll absorption to plant cellular reflectance ('red edge'), refractive index discontinuities of plant cellular constituents, absorption by iron rich soils, or absorption by solid water or ice constituents.

Figure 1 shows the nine standard spectra of surface reflectivity used in the simulations taken from the ASTER spectral library [1]. There are distinct spectral variations for different types of the considered targets. However, within the range between 880nm and 910nm the spectral variation of surface reflectance is up to +/- 12%. Since variations in surface albedo for optical thin atmospheres directly result in variations of the measured signal, even small variations in surface albedo slope may cause significant systematic deviations of the retrieved water vapour content. To account for variations in surface albedo slope, the ratio between the spectral reflectance at 900nm and 885nm is used.
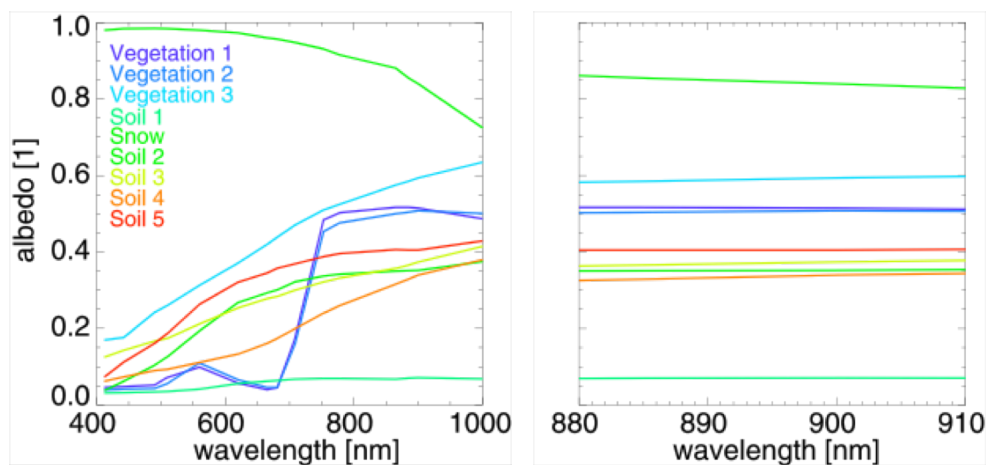
Figure 1: Nine standard albedo spectra used for the regression to estimate the surface albedo at 900nm (left panel). The right panel shows a zoom for the spectra ranging from 880nm to 910nm.

3.1.6. Inverse model parameterization

There are different methods to achieve the water vapour content from radiance measurements. Often used look-up table (LUT) approaches uses the results of RT simulations, containing the TOA radiances, the observing geometry as well the environmental data (spectral surface albedo, wind speed, surface pressure) as entry data. In turn each entry data point is linked to a corresponding output data point (IWV). For the task of water vapour retrieval the "best matching" entry has to be found between the input data and the look-up table data. Since this has to be performed for millions of MERIS pixels, which is very inefficient, the LUT approach was approximated by a non-parametric neural network approach. The neural network is serving as an inversion model. Its free parameters are estimated during a supervised learning procedure based on the samples pulled randomly from the RT simulations described above. Samples pulled out from the simulated data set are present to the network and its output is compared against the expected output as given in the database. This has to be done sequently for all datasets until the difference between the network output and the expected output is minimal. We used the back-propagation algorithm [19] for the network training.

The network applied here consists of three layers of neurons, an input layer, a hidden layer and an output layer (see Figure 6). It had six input and one output neuron(s), each connected to the 60 hidden neurons. This allows performing a highly non linear function approximation. The six input neurons were associated to the input parameters, as defined in table 3, while the output neuron was associated to the integrated water vapour.
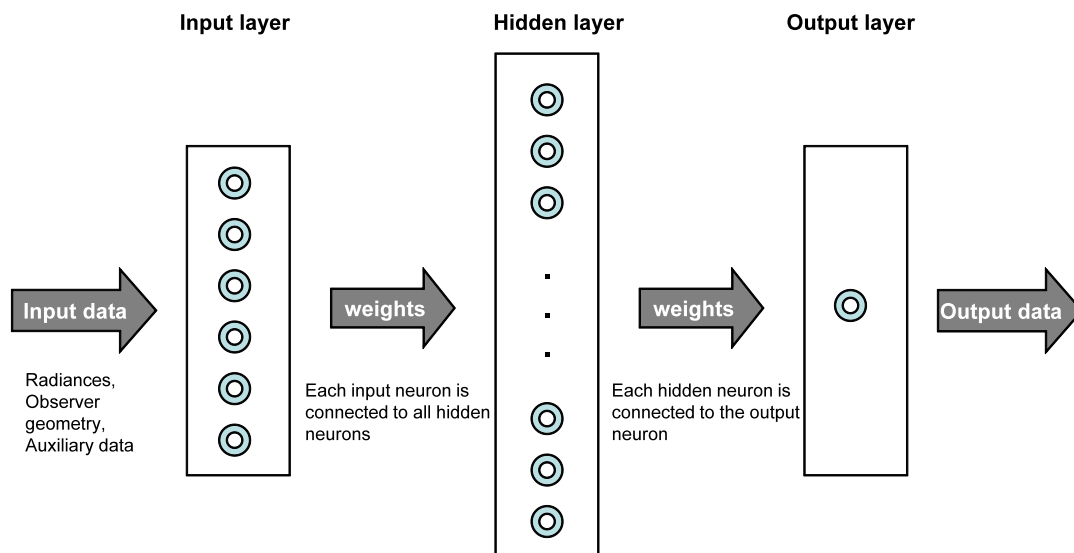

Figure 2: Scheme of the proposed neural network for water vapour retrieval

3.2. The water vapour over land algorithm

In this section we describe the input and output of the water vapour over land artificial neural network (ANN), which is used for the retrieval of integrated water vapour over land areas. All required parameters are tabulated in Table 3. The output of the ANN is the integrated columnar water vapour content over cloud free land areas.

3.2.1. Input to the water vapour over land ANN

The input is a 10 element-tuple of floats containing:

1. $\cos(\theta_{sun})$ the cosine of the sun zenith angle
2. $\cos(\theta_{view})$ the cosine of the viewing zenith angle
3. $\sin(\theta_{view}) \cos(\varphi_{diff})$ the azimuth difference in Cartesian coordinates. φ_{diff} is defined as in MOMO (opposite to the MERIS ground-segment definition).
4. L^N_{14} the radiance in channel M14. The radiance is normalized by the solar constant S^0: $L^N_{14}=L_{14}/S^0_{14}$
5. $\rho_{15/14}=\alpha_{15}/\alpha_{14}$ the surface albedo ratio of M15 and M14. This value will be provided as an auxiliary data file.
6. τ_{H2O} the estimated optical depth of water vapour: $\tau_{H2O}= -\ln(L^N_{15}/ L^N_{14})$, $L^N_X=L_x/S^0_X$
7. L^N_{10} the radiance in channel M10. The radiance is normalized by the solar constant S^0: $L^N_{10}=L_{10}/S^0_{10}$
8. τ_{O2} the estimated optical depth of oxygen: $\tau_{O2}= -\ln(L^N_{11}/ L^N_{10})$, $L^N_X=L_x/S^0_X$
9. λ_{11} the central wavelength of band M11
10. p_{surf} the real surface pressure of the pixel

3.2.2. Definition of auxiliary data

This section describes the surface albedo ratio auxiliary data. There are two ways to retrieve the ratio $\rho_{19/18}$:

1. read it from the FUB-surface albedo product database
2. estimate it from L^N_{12}/ L^N_{14}

The FUB-albedo product is retrieved from the ALBEDOMAP dataset applying some spectral un-mixing. This procedure is very time consuming, because additional atmospheric correction schemes are needed, and therefore not applicable for the NRT processing.

The estimate is a simple linear extrapolation. Both ways are implemented, since both have advantages and disadvantages.

3.2.3. Surface albedo ratio $\rho_{15/14}$ aux data base

The surface albedo database is provided as 12 files (one file for each month of the year) containing 7200x3600 values. The first pixel centre is at (-179.975°W, 89.975°N). The

projection is a simple latitude/longitude with pixel differences of (0.049993056°, 0.049993056°). Thus the last pixel is at (179.975°E, 89.975°S). The database is provided as a part of three FUB albedo products (bs_albedo_M12, bs_albedo_M15 and ratio_bs_albedoM15/M14) as a DIMAP 2.3.0 data format. If the database contains no data the albedo ratio is estimated by linear extrapolation from $L^N_{12}/$ L^N_{14} described in the next subchapter.

3.2.4. Estimation of surface albedo ratio

The needed surface albedo ratio $\rho_{15/14}$ can be estimated by a linear extrapolation from $L^N_{12}/$ L^N_{14}:

$$\alpha_{12} = L_{12} * \pi / \cos(\theta_{sun})$$

$$\alpha_{14} = L_{14} * \pi / \cos(\theta_{sun})$$

$$\alpha_{15} = [7/4 * [\alpha_{14} - \alpha_{12}]] + \alpha_{12}$$

$$\boldsymbol{\rho_{15/14} = \alpha_{15} / \alpha_{14}}$$

IN	Parameter	TYP		Min	Max	Units
1	cosine of the sun zenith angle	**float**	$\cos(\theta_{sun})$	3.42E-01	9.48E-01	**1**
2	cosine of the viewing zenith angle	**float**	$\cos(\theta_{view})$	6.80E-01	1.00E+00	**1**
3	azimuth difference in Cartesian coordinates	**float**	$\sin(\theta_{view}) \cos(\varphi_{diff})$	-7.33E-01	7.33E-01	**1**
4	MERIS radiance in channel 14	**float**	L^N_{14}	4.10E-03	1.98E-01	**sr^{-1}**
5	surface albedo ratio	**float**	$\rho_{15/14}$	8.99E-01	1.07E+00	**1**
6	estimated optical depth of water vapour	**float**	τ_{H2O}	3.56E-02	8.63E-01	**1**
7	MERIS radiance in channel 10	**float**	L^N_{10}	5.40E-03	1.97E-01	**sr^{-1}**
8	Estimated optical depth of oxygen	**float**	τ_{O2}	1.67E+00	9.07E+00	**1**
9	MERIS central wavelength of band 11	**float**	λ_{11}	7.59E+02	7.65E+02	**Nm**
10	surface pressure	**float**	p_{surf}	6.48E+02	1.02E+03	**hPa**

Table 3: Input parameters for the water vapour over land ANN

3.2.5. Output of the water vapour ANN

The output of the water vapour network is a "float array" of the dimension (1) or (*,1).

Out	Parameter	Type		Minimum	Maximum	Units
1	Integrated columnar water vapour content over cloud free land areas	**float**	IWV	0.012	76.2	**kg/m²**

Table 4: Output parameters for the water vapour over land ANN

3.3. The water vapour over ocean algorithm

In this section we describe the input and output of the water vapour over ocean ANN which is used for the retrieval of integrated water vapour over ocean.

3.3.1. Input to the water vapour over ocean ANN

The input is a 5 element-tuple of floats containing:

1. the windspeed calculated from the zonal (u) and meridional (v) wind components: wind=Sqrt(u^2+v^2)
2. $\sin(\theta_{view}) \cos(\varphi_{diff})$ the azimuth difference in Cartesian coordinates. φ_{diff} is defined as in MOMO (opposite to the MERIS ground-segment definition).
3. $\cos(\theta_{sun})$ is the cosine of the sun zenith angle
4. $\cos(\theta_{view})$ is the cosine of the viewing zenith angle
5. T_{H2O} the estimated water vapour transmission: $T_{H2O}= \ln(L^N_{15}/ L^N_{14})$, $L^N_X=L_X/S^0_X$

IN	Parameter	TYP		Min	Max	Units
1	wind speed	**float**	wind	3.75E-02	1.84E+01	**m/s**
2	azimuth difference in Cartesian coordinates	**float**	$\sin(\theta_{view}) \cos(\varphi_{diff})$	-6.33E-01	6.31E-01	**Dimless**
3	cosine of the viewing zenith angle	**float**	$\cos(\theta_{view})$	7.73E-01	1.00E+00	**Dimless**
4	cosine of the sun zenith angle	**float**	$\cos(\theta_{sun})$	1.60E-01	9.26E-01	**Dimless**
5	estimated water vapour transmission	**float**	T_{H2O}	-6.98E-01	-1.25E-01	**Dimless**

Table 5: Input parameters for the water vapour over ocean ANN

15

3.3.2. Output of the water vapour over ocean ANN

The output of the water vapour network is a "float array" of the dimension (1) or (*,1).

Out	Parameter	Type		Minimum	Maximum	Units
1	Integrated columnar water vapour content over ocean	**float**	**IWV**	0.012	76.2	**kg/m²**
	Table 6: Output parameters for the water vapour over land ANN					

3.4. The water vapour over clouds algorithm

In this section we describe the input and output of the water vapour over clouds ANN which is used for the retrieval of integrated water vapour over clouds.

3.4.1. Input to the water vapour over clouds ANN

The input is a 6 element-tuple of floats containing:

1. L^N_{14} the radiance in channel 14. The radiance is normalized by the solar constant S^0: $L^N_{14} = L_{14}/S^0_{14}$
2. T_{H20} the estimated water vapour transmission: $T_{H20} = \ln(L^N_{15}/L^N_{14})$, $L^N_X = L_X/S^0_X$
3. $\cos(\theta_{sun})$ the cosine of the sun zenith angle
4. $\cos(\theta_{view})$ the cosine of the viewing zenith angle
5. $\sin(\theta_{view}) * \varphi_{diff}$ the azimuth difference φ_{diff} is defined as in MOMO (opposite to the MERIS ground-segment definition).
6. α_{14} the surface albedo of MERIS channel M14. This value will be provided as an auxiliary data file

IN	Parameter	TYP		Min	Max	Units
1	MERIS radiance in channel 14	**float**	L^N_{18}	9.30E-03	3.70E-01	**sr⁻¹**
2	estimated water vapour transmission	**float**	T_{H20}	-8.05E-01	8.90E-03	**1**
3	cosine of the sun zenith angle	**float**	$\cos(\theta_{sun})$	3.42E-01	9.75E-01	**1**
4	cosine of the viewing zenith angle	**float**	$\cos(\theta_{view})$	6.04E-01	1.00E+00	**1**
5	azimuth difference in Cartesian coordinates	**float**	$\sin(\theta_{view}) * \varphi_{diff}$	0.00E+00	1.43E+02	**1**
6	surface albedo	**float**	ρ_{14}	0.00E+00	1.00E+00	**1**
	Table 7: Input parameters for the water vapour over clouds ANN					

3.4.2. Output of the water vapour over clouds ANN

The output of the water vapour network is a "float array" of the dimension (1) or (*,1).

Out	Parameter	Type		Minimum	Maximum	Units
1	Integrated columnar water vapour content over clouds	**float**	**IWV**	0.012	76.2	**kg/m²**
	Table 8: Output parameters for the water vapour over land ANN					

17

4. PRACTICAL CONSIDERATIONS

4.1. Azimuth difference transformation of the MERIS data

The different ANNs has been trained with simulated azimuth differences in the range between [−180°,+180°]. An azimuth difference of 0° means looking into the forward scattering direction while a difference of ±180° is looking into the backscattering direction. This range for the azimuth differences has to be used when applying the approach to MERIS data. The azimuth difference should be calculated according to the following steps.

1: calculate azimuth difference $\varphi_{diff, MERIS}$ of observer and sun azimuth from the MERIS data file with:

$$\varphi_{diff, MERIS} = \varphi_{view} - \varphi_{sun} \tag{1}$$

2: transform the azimuth difference to the interval [−180, +180]:

$$\text{if } \varphi_{diff, MERIS} \leq -180° \text{ then } \varphi_{diff, MERIS} = 360° + \varphi_{diff, MERIS} \tag{2}$$
$$\text{if } \varphi_{diff, MERIS} > +180° \text{ then } \varphi_{diff, MERIS} = -360° + \varphi_{diff, MERIS} \tag{3}$$

3: transform $\varphi_{diff,MERIS}$ to azimuth definition of the inversion model $\varphi_{diff,ANN}$ with:

$$\text{if } \varphi_{diff, MERIS} \geq 0° \text{ then } \varphi_{diff, ANN} = 180° - \varphi_{diff, MERIS} \tag{4}$$
$$\text{if } \varphi_{diff, MERIS} < 0° \text{ then } \varphi_{diff, ANN} = -180° - \varphi_{diff, MERIS} \tag{5}$$

The azimuth difference $\varphi_{diff,ANN}$ as specified in (4−5) is needed as input to the network.

4.2. Observer geometry transformation of MERIS data

Moreover, the observer geometry needs to be transformed to avoid inversion ambiguities. The parameters x, y, z in (6−8) are further on used as input to the networks.

$$x = \cos(\theta_{sun}) \tag{6}$$
$$y = \cos(\theta_{view}) \tag{7}$$
$$z = \sin(\theta_{view}) \cos(\varphi_{diff, ANN}) \tag{8}$$

5.   VALIDATION AND ERROR ESTIMATES OF THE MERIS WATER VAPOUR RETRIEVAL

For a validation and an error estimate of the proposed water vapour retrieval thousands of MERIS scenes have been analysed and the derived water vapour contents have been compared with the integrated water vapour derived from Microwave Radiometer (MWR) measurements on the ARM-SGP site in Oklahoma/USA and with ground based GPS-measurements. The validation period last for three years from January 2003 to December 2005. In the next sections the validations results are shown.

### 5.1.   Validation with Microwave Radiometers

The Microwave Radiometer (MWR) receives microwave radiation from the sky at 23.8 GHz and 31.4 GHz. Measurements in these two frequencies allow us to determine water vapour and liquid water along a selected path. The accuracy of water vapour retrievals from MWR measurements is within the order of $0.3 kg/m^2$ [25].

For this validation exercise the data were collected from four different microwave radiometers on the ARM-SGP site in Oklahoma (Figure 3). The triangles flag the geographical position of the stations. The size of the triangle indicates the number of observations that were achieved for the comparison while the colour denotes the height of the station. The microwave radiometer measurements have been provided with a temporal resolution of one second. For each case, in which microwave radiometer and MERIS data have been available and the appropriate MERIS pixel was cloud free, the microwave radiometer measurement was compared to the MERIS pixel. 794 collocations were found within the time frame of three years. The validation result is presented in a scatter plot shown in Figure 3. The one by one line is plotted in black and the regression line in red, colours denote data density with small values in blue and large values in red. The agreement between MERIS and microwave radiometer measurements is very high, with a root mean square deviation of $1.64 kg/m^2$ and a bias of $-0.03 kg/m^2$.

5.2.   Validation with GPS

A second validation was performed using ground based Global Positioning System (GPS) measurements. For the validation GPS measurements provided by the GFZ Potsdam were used. The data were available for 153 Stations located in Central Europe shown in Figure 4. The size of the triangles indicates the number of valid observations that were used for the comparison. The height of each GPS station is given by the colour of the triangle. The water vapour product is generated each hour with a 30-minute time resolution and an accuracy of $+/-1-2 kg/m^2$ [26]. For each day in which MERIS data were available, the satellite pixels closest to each GPS station were used for comparison. Cloud free pixels were taken into account, when the time difference between the MERIS overpass and the GPS measurements was less than 30 minutes. 4424 collocations were found. The result for the validation of all 4424 collocations is presented in Figure 4. The one by one line is plotted in black and the regression line is in red, the colours denote the data density. The agreement between MERIS and GPS measurements is very high, with a root mean square deviation of $1.22 kg/m^2$ and a bias of $0.97 kg/m^2$. These values are in the range of the accuracy of the GPS-water vapour product. The bias is higher compared to the validation to microwave radiometer, the root mean square error is slightly below. In spite of the

very good comparison, the cause of the bias between MERIS and GPS water vapour retrieval has to be inspected in more detail and might be subject of further investigations.
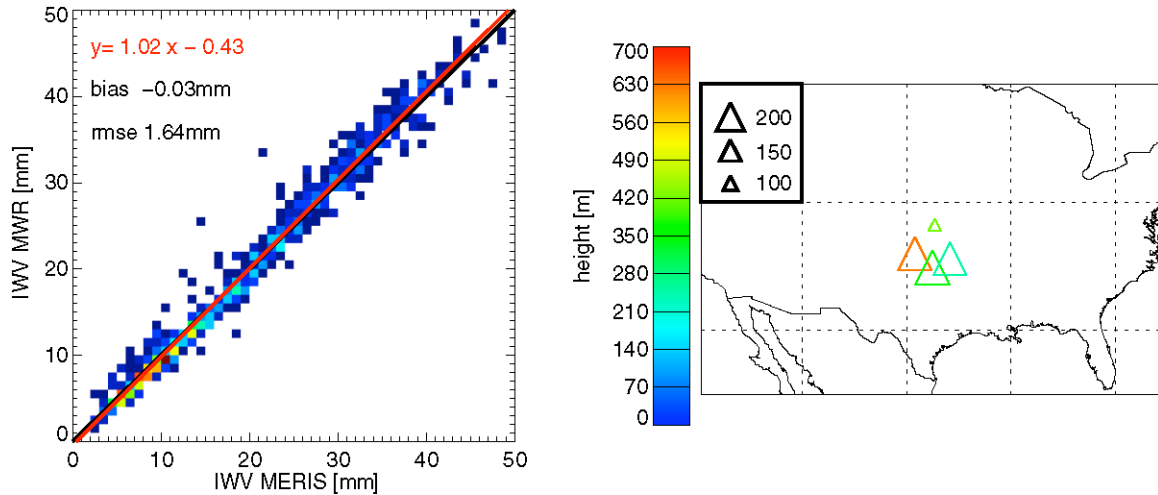
Figure 3: Integrated water vapour from MERIS and Microwave Radiometer at ARM-SGP site. The upper panel show the scatter plot of 794 collocations for a period of three years. The colour indicates the number of collocations with high values in red and small values in blue. The lower panel illustrates the location of the four used microwave radiometer stations. The size of the triangles denotes the number of observations used for the comparison, while the colour indicates the height of the MWR-station.
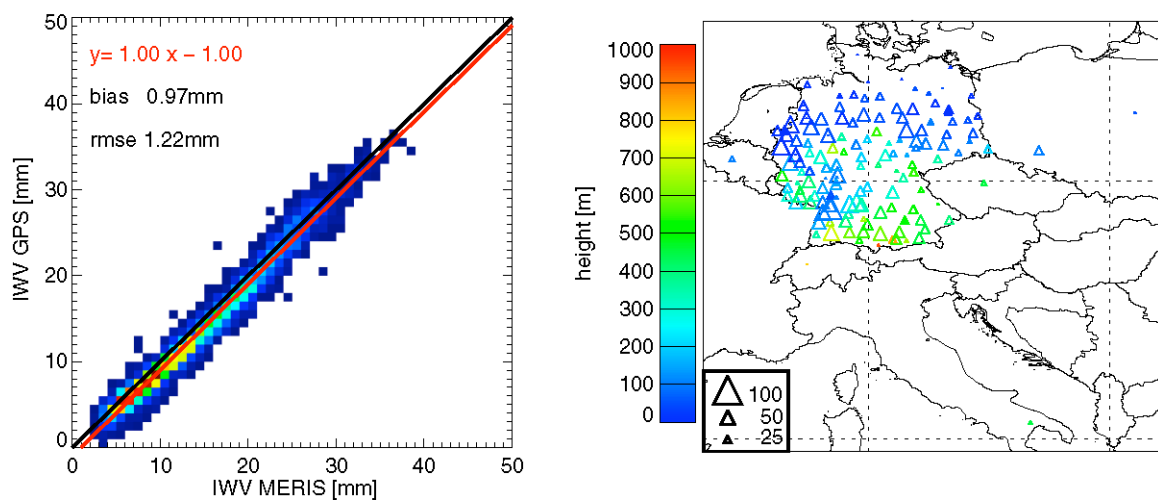
Figure 4: Integrated water vapour from MERIS and from GPS measurements located in Central Europe. The upper panel shows the scatter plot of 4424 collocations for a period of three years. The colour indicates the number of collocations with high values in red and small in blue. The lower panel illustrates the location of the 153 used GPS-receivers. The size of the triangle denotes the number of observations used for the comparison, while the colour indicates the height of the GPS-station.

5.3. Validation summary

All validation results are summarized in Table 9. For each validation dataset the root mean square error as well as the bias was calculated. The agreement between MERIS and in situ measurements is very high. The best validation result is observable for the microwave radiometers with a root mean square deviation of 1.64 kg/m^2 and a bias of -0.03 kg/m^2. For the comparison with GPS measurements a bias of 1 kg/m^2 has been achieved. This indicates a systematic overestimation of the MERIS water vapour measurements in comparison with GPS measurements. The overestimation of MERIS measurements is not observable for the microwave radiometer validation results. The validation results show the high accuracy of the proposed water vapour algorithm.

	rmse [kg/m^2]	bias [kg/m^2]
MWR - data	1.64	-0.03
GPS - data	1.22	1.00

Table 4: Summary of all validation analysis performed over three years from January 2003 to December 2005.

Since the observed water vapour contents does not cover values higher than 40kg/m^2, further investigations are needed, keeping in mind that globally available radio-sonde measurements do not provide the required accuracy in the water vapour estimates. Additionally, the bias between GPS and MERIS water vapour retrievals has to be invested.

This ATBD relies on the total water vapour retrieval as provided for the MERIS ground-segment (MEGS 8.0).

6. REFERENCES

[1]   A.M. Baldridge, S.J. Hook, C.I. Grove, and G. Rivera. The aster spectral library version 2.0. *Remote Sensing of Environment*, 113(4):711 – 715, 2009.

[2]   B. Bartsch, S. Bakan, and J. Fischer. Passive remote sensing of the atmospheric water vapour content above land surfaces. *Advances in Space Research*, 18:25–28, 1996.

[3]   R. Bennartz and J. Fischer. A modified k-distribution approach applied to narrow band water vapour and oxygen absorption estimates in the near infrared. *Journal of Quantitative Spectroscopy and Radiative Transfer*, 66:539–553, September 2000.

[4]   R. Bennartz and R. Preusker. Representation of the photon pathlength distribution in a cloudy atmosphere using finite elements. *Journal of Quantitative Spectroscopy and Radiative Transfer*, 98:202–219, March 2006.

[5]   R. E.; Myrick D. L.; Stacy K.; Jones W. T. Bowker, D. E.; Davis. Spectral reflectances of natural targets for use in remote sensing studies. *NASA-RP-1139*, 1985.

[6]   F. Fell and J. Fischer. Numerical simulation of the light field in the atmosphere-ocean system using the matrix-operator method. *Journal of Quantitative Spectroscopy and Radiative Transfer*, 69:351–388, May 2001.

[7]   J. Fischer. High Resolution Spectroscopy for Remote Sensing of Physical Cloud Properties and Water Vapour. *In: Current Problems in Atmospheric Radiation, ED. Lenoble and Geleyn, Deepak Publishing*, pages 151–156, 1988.

[8]   J. Fischer and H. Graßl. Detection of Cloud-Top Height from Backscattered Radiances within the Oxygen A Band. Part 1: Theoretical Study. *J. Appl. Meteor.*, 30(9):1245–1259, 1991.

[9]   G. GENDT, Galina DICK, Christoph REIGBER, Maria TOMASSINI, Yanxiong LIU, and Markus RAMATSCHI. Near real time gps water vapor monitoring for numerical weather prediction in germany. *Journal of the Meteorological Society of Japan*, 82(1B):361–370, 2004.

[10]   Yong Han and E.R. Westwater. Remote sensing of tropospheric water vapor and cloud liquid water by integrated ground-based sensors. *Journal of Atmospheric and Oceanic Technology*, 12(5):1050–1059, October 1995.

[11]   J. T. Kiehl and K. E. Trenberth. Earth's Annual Global Mean Energy Budget. *Bulletin of the American Meteorological Society, vol. 78, Issue 2, pp.197-197*, 78:197–197, February 1997.

[12]   J. Liljegren. Automatic self-calibration of arm microwave radiometers. *Microwave Radiometry and Remote Sensing of the Earths Surface and Atmosphere*, pages 433–443, 2000.

[13]   R. Lindstrot, R. Preusker, Th. Ruhtz, B. Heese, M. Wiegner, C. Lindemann, and J. Fischer. Validation of MERIS cloud top pressure using airborne lidar measurements. *Journal of Applied Meteorology and Climatology*, **45** (12), 1612-1621, 2006.

[14]   G. N. Plass, G. W. Kattawar, and F. E. Catchings. Matrix operator theory of radiative transfer, 1: Rayleigh scattering. *Applied Optics*, 12:314–329, 1973.

[15]   R. Preusker, J. Fischer, P. Albert, and R. Bennartz. Cloud top pressure retrieval using the oxygen A-band in the IRS-3 MOS instrument . Int. J. Remote Sensing, **28,** 1957-1967, 2007.

[16]   R. Preusker and R. Lindstrot. Remote sensing of cloud-top pressure using moderately resolved measurements within the oxygen A band. *J. Appl. Meteor. Clim.*, 48, 1562-1574, 2009.

[17]   V. Ramanathan, B. R. Barkstrom, and E. F. Harrison. Climate and the earth's radiation budget. *Physics Today*, 42:22–33, May 1989.

[18]   L. S. Rothman, A. Barbe, D. Chris Benner, L. R. Brown, C. Camy-Peyret, M. R. Carleer, K. Chance, C. Clerbaux, V. Dana, V. M. Devi, A. Fayt, J. M. Flaud, R. R. Gamache, A. Goldman, D. Jacquemart, K. W. Jucks, W. J. Lafferty, J. Y. Mandin, S. T. Massie, V. Nemtchinov, D. A. Newnham, A. Perrin, C. P. Rinsland, J. Schroeder, K. M. Smith, M. A. H. Smith, K. Tang, R. A. Toth, J. Vander Auwera, P. Varanasi, and K. Yoshino. The hitran molecular spectroscopic database: edition of 2000 including updates through 2001. *Journal of Quantitative Spectroscopy and Radiative Transfer*, 82(1-4): 5 – 44, 2003. The HITRAN Molecular Spectroscopic Database: Edition of 2000 Including Updates of 2001.

[19]   D. E. Rumelhart, G. E. Hinton, and R. J. Williams. Learning representations by back-propagating errors. *Nature*, 323:533–536, October 1986.

[20]   F. Santer, R. Zagolski, D. Ramon, J. Fischer, and P. Dubuisson. Uncertainties in radiative transfer computations: consequences on the MERIS products over land. *International Journal of Remote Sensing*, 26(20):4597 – 4626, 2005.

[21]   D. Starr and S. H. Melfi. The Role of Water Vapour in Climate, A Strategic Research Plan for the Proposed GEWEX Water Vapour Project (GVaP). *NASA Conference Publication*, 3210:60 pp., 1991.

[22]   K. E. Trenberth, J. Fasullo, and L. Smith. Trends and variability in column-integrated atmospheric water vapor. *Climate Dynamics*, 24:741–758, June 2005.

[23]   D. D. Turner, B. M. Lesht, S. A. Clough, J. C. Liljegren, H. E. Revercomb, and D. C. Tobin. Dry bias and variability in vaisala rs80-h radiosondes: The arm experience. *Journal of atmospheric and oceanic technology*, vol. 20, no1:117–132, 2003.

[24]   J. Luo, T. Vonder Haar, T., Forsythe, D.L. Randel, and S. Woo. WATER VAPOR TRENDS AND VARIABILITY FROM THE GLOBAL NVAP DATASET. *16th Symposium on Global Change and Climate Variations*, 2005.

[25]   D.D. Turner, B. M. Lesht, S. A. Clough, J. C. Liljegren, H. E. Revercomb, and D. C. Tobin. Dry bias and variability in vaisala rs80-h radiosondes: The arm experience. Journal of atmospheric and oceanic technology, vol. 20, no1, 117_132, 2003.

[26]   Gendt, G., G. Dick, C. Reigber, M. Tomassini, Y. Liu, and M. Ramatschi, 2004: Near real time gps water vapor monitoring for numerical weather prediction in germany. Journal of the Meteorological Society of Japan, 82, 361_370.